

Article

Preparation of $\text{Cu}_3\text{N}/\text{MoS}_2$ Heterojunction through Magnetron Sputtering and Investigation of Its Structure and Optical Performance

Liwen Zhu, Xiu Cao, Chenyang Gong, Aihua Jiang, Yong Cheng and Jianrong Xiao * 

College of Science, Guilin University of Technology, Guilin 541004, China; zhuliwen1995@163.com (L.Z.); caoxiu23@163.com (X.C.); g6288170@163.com (C.G.); jah@glut.edu.cn (A.J.); chengyong@glut.edu.cn (Y.C.)

* Correspondence: xjr@glut.edu.cn

Received: 25 March 2020; Accepted: 13 April 2020; Published: 16 April 2020



Abstract: $\text{Cu}_3\text{N}/\text{MoS}_2$ heterojunction was prepared through magnetron sputtering, and its optical band gap was investigated. Results showed that the prepared $\text{Cu}_3\text{N}/\text{MoS}_2$ heterojunction had a clear surface heterojunction structure, uniform surface grains, and no evident cracks. The optical band gap (1.98 eV) of $\text{Cu}_3\text{N}/\text{MoS}_2$ heterojunction was obtained by analyzing the ultraviolet-visible transmission spectrum. The valence and conduction band offsets of $\text{Cu}_3\text{N}/\text{MoS}_2$ heterojunction were 1.42 and 0.82 eV, respectively. The Cu_3N film and multilayer MoS_2 formed a type-II heterojunction. After the two materials adhered to form the heterojunction, the interface electrons flowed from MoS_2 to Cu_3N because the latter had higher Fermi level than the former. This behavior caused the formation of additional electrons in the Cu_3N and MoS_2 layers and the change in optical band gap, which was conducive to the charge separation of electrons in MoS_2 or MoS_2 holes. The prepared $\text{Cu}_3\text{N}/\text{MoS}_2$ heterojunction has potential application in various high-performance photoelectric devices, such as photocatalysts and photodetectors.

Keywords: $\text{Cu}_3\text{N}/\text{MoS}_2$ films; heterojunction; magnetron sputtering; photocatalysis

1. Introduction

Environmental problems have worsened due to the rapid consumption of fossil fuels. Thus, efficient, energy-saving, and environmentally friendly methods must be developed to solve various pollution problems [1]. Among them, photocatalysis is a widely used technology in solar energy conversion and shows good potential [2,3]. Other available methods are sewage treatment [4,5] and dye degradation [6,7]. Heterojunctions formed with 2D materials and other semiconductors have recently attracted attention from researchers due to their various potential applications. Many heterojunction materials, including semiconductors/semiconductors, metals/semiconductors, molecules/semiconductors [8,9], and multiple heterojunctions [10], have been used in photocatalysis and achieved considerable success. Heterojunction photocatalysts typically have the following advantages: strong light absorption [11], efficient charge separation and transport [12], cocatalyst effect, and strong light absorption stability [13].

Among these heterojunctions, $\text{Cu}_3\text{N}/\text{MoS}_2$ shows promise as a photocatalyst because Cu_3N is an outstanding semiconductor material that can substantially enhance the photoelectric performance of MoS_2 or introduce new functions into such heterojunctions. As a typical transition metal sulfide, MoS_2 has a S–Mo–S sandwich structure combined by the van der Waals force [14,15]. Given its unique structure and photoelectric properties, MoS_2 has attracted considerable attention from scholars [16,17] and has been widely investigated for thin film transistors [18,19], photodetectors [20,21], and solid lubrication [22,23]. Owing to its adjustable band gap, MoS_2 can be combined with

many types of semiconductors to enhance light absorption from the ultraviolet to visible light regions [7,24], increase the separation and lifetime of charge carriers, and provide potential applications in visible-light catalysis [25,26]. Cu_3N is a widely used material because of its metal-to-semiconductor properties [27,28]. Cu_3N has been proposed for battery materials [2,29], catalyst additives [30], spin tunnel junction [31], memory [32], and electric transport materials [33] due to its wide range of optical band gap, low temperature of thermal decomposition, and excellent chemical activity.

Heterojunctions, such as MoS_2/ZnO [13], $\text{MoS}_2/\text{TiO}_2$ [11], and TiO_2/WO_3 [34], remarkably improve the electrical conductivity and optical properties of materials. However, to the best of our knowledge, $\text{Cu}_3\text{N}/\text{MoS}_2$ heterojunction materials have not been investigated. In addition, the complicated and limited preparation of most heterogeneous structures usually involves many steps and thus is not conducive to large-scale operations. Therefore, a simple and effective preparation method for $\text{Cu}_3\text{N}/\text{MoS}_2$ heterojunction is needed. Magnetron sputtering has become a popular technique due to its advantages of fast deposition speed, wide target range, good sample quality, and controllable parameters.

Our previous work investigated the photocatalytic properties of $\text{Cu}_3\text{N}/\text{MoS}_2$ composite films. In contrast, in this study, we made a more detailed and accurate study of the $\text{Cu}_3\text{N}/\text{MoS}_2$ heterojunction, and explained in more depth the reasons for the change in the band gap of the $\text{Cu}_3\text{N}/\text{MoS}_2$ heterojunction. Through the corresponding calculation, we found that the $\text{Cu}_3\text{N}/\text{MoS}_2$ heterojunction has better optical performance. In this study, $\text{Cu}_3\text{N}/\text{MoS}_2$ heterojunction was fabricated through magnetron sputtering, and its crystal structure, chemical composition, surface morphology, and band gap structure were explored.

2. Experimental

$\text{Cu}_3\text{N}/\text{MoS}_2$ heterojunctions were prepared on single-crystal silicon (100) and quartz substrates by using RF magnetron sputtering (JGP-450a, SKY Technology Development Co., Ltd, Shenyang, China). First, the silicon and quartz wafer substrates were separately sonicated in an acetone and ethanol solution for 15 min, rinsed with deionized water, and dried for further use. Second, the processed monocrystalline silicon and quartz wafers were placed in the substrate support, the target was installed, and the sputtering chamber was closed. Third, the sputtering chamber was evacuated to 2.5 Pa with a mechanical pump and the vacuum was driven to 1×10^{-4} Pa by using a turbomolecular pump. Before the experiment, the target was presputtered in Ar atmosphere for 10 min and the surface of the target was cleaned to remove the oxide. Fourth, the MoS_2 layer was deposited on the substrate using high-purity molybdenum disulfide target (99.99%, Beijing Jingmai Zhongke Material Technology Co., Ltd., Beijing, China) in Ar atmosphere at room temperature. Total gas flow rate, vacuum chamber pressure, power, and sputtering time were set to 40 sccm, 1.0 Pa, 150 w, and 2 and 3.5 min, respectively. Fifth, a Cu_3N layer was deposited on the MoS_2 layer with a sputtering time of 2 min using a copper target (99.99%, Beijing Jingmai Zhongke Material Technology Co., Ltd., Beijing, China). Total gas flow rate, flow ratio of N_2 and Ar, vacuum chamber pressure, power, and sputtering time were set to 40 sccm, 3:1, 1 Pa, 150 W, and 1.5 min, respectively. Under the same experimental conditions, a pure Cu_3N layer was deposited on the blank substrate for 3.5 min. The deposition rates of MoS_2 and Cu_3N layers are 12 and 13.3 nm/min, respectively. The diameter of molybdenum disulfide target and copper target are both 60 mm. The sputtering time for the heterojunction in the scanning electron microscopy (SEM, Hitachi, Tokyo, Japan) was enlarged 10 times, and the rest of the conditions remained unchanged to easily observe the heterojunction structure.

The surface morphology of heterojunction was characterized with a field emission scanning electron microscope (S-4800, Hitachi, Tokyo, Japan). The crystal structure of heterojunction was characterized using X-ray diffractometry (XRD, X'Pert PRO, PANalytical, Holland). Elemental characterization was conducted via X-ray photoelectron spectroscopy (XPS, Escalab, Thermo Fisher Scientific, MA, USA). The optical band gap of heterojunction was investigated with an ultraviolet-visible (UV-vis) spectrometer (UV-2600/2700, Shimadzu, Kyoto, Japan).

3. Results and Discussion

The XRD test patterns of MoS₂ layer, Cu₃N layer, and Cu₃N/MoS₂ heterojunction are shown in Figure 1. The 2θ in the MoS₂ (002), (100), (101), and (110) crystal planes was found at 14.55°, 32.3°, 36.5°, and 49.4°, respectively [22,35]. The absence of other impurity peaks in the spectrum indicated the high purity of the obtained MoS₂. Moreover, the sharp diffraction peak of MoS₂ revealed the good crystallinity of MoS₂. The average grain size of the heterojunction was 14.9 nm, which was smaller than the grain size observed in the SEM image. This may have been because the size of the grain aggregate observed by the SEM was not the size of the single grain; therefore, the particle size value observed by SEM was often larger than the calculated value. When the Cu₃N layer was deposited on the MoS₂ layer to form the Cu₃N/MoS₂ heterojunction, the sample still showed reflection on the (100), (101), and (110) crystal planes of MoS₂. However, the intensity of the (100), (101), and (110) crystal planes of MoS₂ in the Cu₃N/MoS₂ heterojunction was weaker than that in the pure MoS₂ layer, indicating the reduced crystal quality of the MoS₂ layer after Cu₃N deposition. Compared with that of the pure Cu₃N layer, the strength of the (100) and (200) crystal planes of Cu₃N in the Cu₃N/MoS₂ heterojunction decreased, possibly due to the interdiffusion of atoms that occurred at the interface between MoS₂ and Cu₃N and led to the reduced quality of heterogeneous crystals.

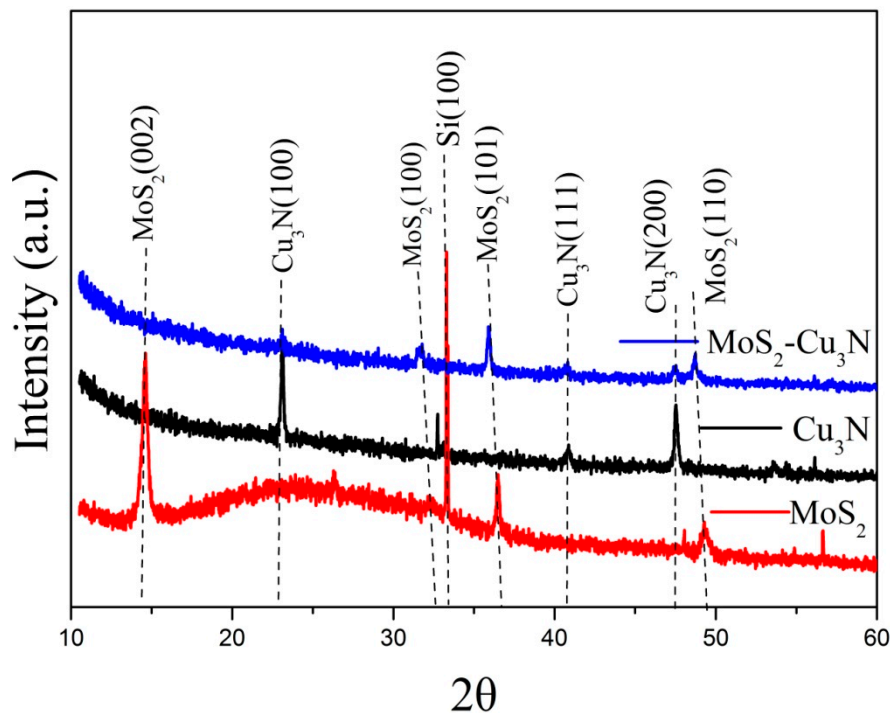


Figure 1. XRD patterns of the MoS₂ layer, Cu₃N layer, and Cu₃N/MoS₂ heterojunction.

The surface and cross-sectional morphology of the Cu₃N/MoS₂ heterojunction are shown in Figure 2. This surface of the MoS₂ layer was generally smooth and flat with block particles of uniform size and no evident cracks. These characteristics were beneficial to the growth of the Cu₃N layer on the surface of the MoS₂ layer. Figure 2b shows the thickness of the heterojunction. The MoS₂ and Cu₃N layers had a thicknesses of approximately 300 and 200 nm, respectively. The boundary between the layers clearly showed the heterojunction structure. The relationship between the film deposition thickness and deposition time suggested that the Cu₃N/MoS₂ heterojunction was approximately 50 nm-thick.

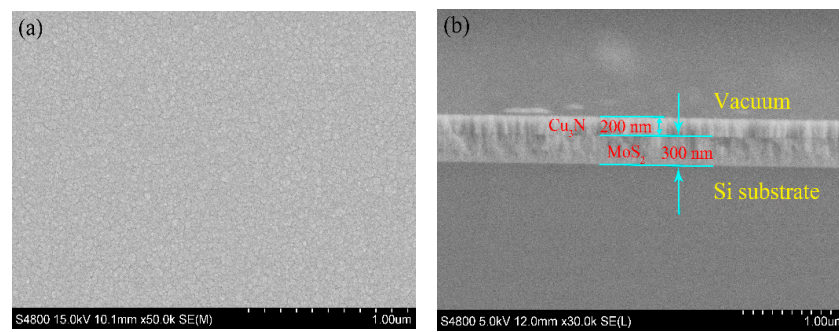


Figure 2. SEM image of $\text{Cu}_3\text{N}/\text{MoS}_2$ heterojunction deposited on silicon wafer: (a) surface of the MoS_2 layer and (b) cross-section of the heterojunction.

The distribution of elements in the $\text{Cu}_3\text{N}/\text{MoS}_2$ heterojunction and the atomic percentage of each element are shown in Figure 3. EDS data revealed that the ratio of Cu to N atoms in the heterojunction was around 1. Moreover, its chemical ratio differed from the standard ratio of Cu_3N , possibly because of the free Cu atoms in the heterojunction. These free atoms did not combine with the N atoms to form Cu_3N . However, fewer Mo and S atoms were detected on the surface of the heterojunction. The ratio of Mo and S atoms was about 1.87. This phenomenon occurred because MoS_2 can be found in the lower layer, and some Mo atoms in the lower layer had moved to the surface. Meanwhile, the S atoms had difficulty in reaching the surface. The atomic ratio of Cu and N in the film Cu_3N was 1:1, which does not meet the standard atomic ratio of Cu_3N , in which the N element was significantly more than the Cu element. This is because during the deposition process, the ratio of N_2 to Ar was high, and a part of the free N atoms were adsorbed between the crystal grains. However, when $\text{Mo}:\text{S} = 3.11:1.66 = 1:0.53 \approx 1.87:1$, there were fewer S atoms. This may have been because when MoS_2 is deposited, a part of S becomes a single substance to escape, resulting in fewer S atoms. Mo atoms that were not combined into MoS_2 combined with MoO_3 to oxygen (as shown in Figure 4e,f). In addition, the XPS spectrum also proved that there were a large number of Cu^+ , N^- (as shown in Figure 4c,d), and Mo-S bonds (as shown in Figure 4e,f) in the film. It showed that the heterojunction is mainly composed of Cu_3N and MoS_2 , and contains only a small amount of MoO_3 and N atoms, which does not affect the formation of $\text{Cu}_3\text{N}/\text{MoS}_2$ heterojunction. In addition, the Si atoms detected via EDS originated from the monocrystalline silicon substrate.

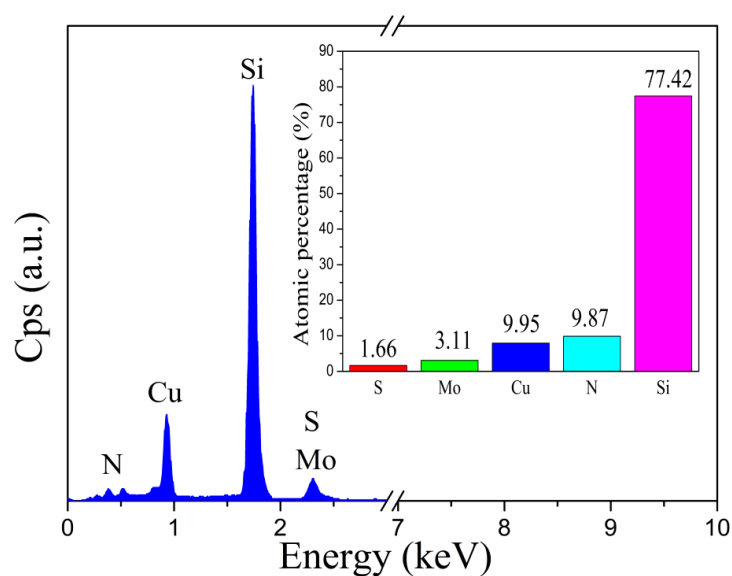


Figure 3. EDS spectrum of the $\text{Cu}_3\text{N}/\text{MoS}_2$ heterojunction.

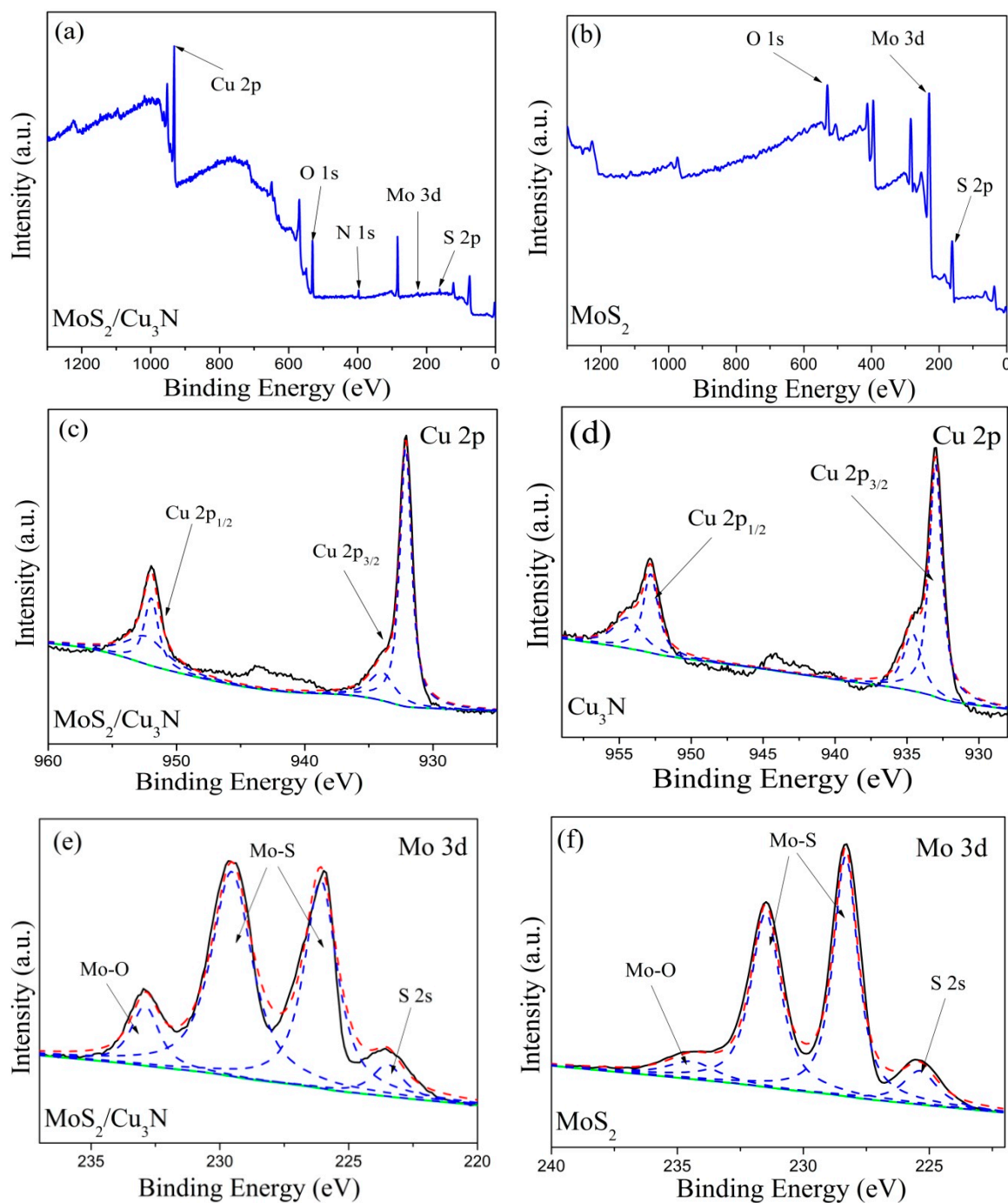


Figure 4. XPS spectrum: (a) total spectrum of the $\text{Cu}_3\text{N}/\text{MoS}_2$ heterojunction, (b) MoS_2 total spectrum, (c) Cu 2p peak fitting in the $\text{Cu}_3\text{N}/\text{MoS}_2$ heterojunction, (d) Cu 2p peak fitting in the Cu_3N layer, (e) Mo 3d peak fitting in the $\text{Cu}_3\text{N}/\text{MoS}_2$ heterojunction, and (f) Mo 3d peak fitting in the MoS_2 layer.

The chemical composition of the $\text{Cu}_3\text{N}/\text{MoS}_2$ heterojunction was characterized using XPS, and the test results are shown in Figure 4. Figure 4a,b illustrates the total spectrum of the $\text{Cu}_3\text{N}/\text{MoS}_2$ heterojunction and MoS_2 thin film, respectively. Figure 4a depicts that the binding energies of the S2p, Mo 3d, N1s, O1s, and Cu2p peaks were 162.6, 227.8, 397.4, 530.5, and 931.3 eV, respectively [15]. Figure 4b shows that the S2p and Mo 3d peaks appeared at the binding energies of 161.5 and 229.5 eV, respectively. The O1s peak appearing in the spectrogram might be due to the inevitable atmospheric pollution in the heterojunction during transfer and testing. However, a weak S2p peak appeared at 162.6 eV possibly due to the trace S atoms sputtered out during the deposition of the remaining

MoS₂ layer in the vacuum chamber, thus causing pollution in the Cu₃N layer. The high intensity peaks with binding energies of 931.1 and 952.1 eV corresponded to the Cu2p_{3/2} and Cu2p_{1/2} orbital peaks, respectively, as shown in Figure 4c. Figure 4d illustrates the fitting of Cu2p peaks in the Cu₃N layer with the Cu2p_{3/2} and Cu2p_{1/2} orbital peaks at the binding energies of 932.81 and 952.76 eV, respectively [27]. In Figure 4c,d, weaker peaks appeared at the binding energies of 933.9, 952.6 eV and 934.5, 954.4 eV, which belong to Cu²⁺, which is caused by the slight oxidation of Cu⁺. Figure 4e,f depicts the Mo3d spectra in the Cu₃N/MoS₂ heterojunction and pure MoS₂ layers, respectively. After the XPS spectrum of Mo3d was fitted, four peaks appeared with different intensities. The two main peaks located at 232.0 and 228.5 eV could be inferred as the Mo3d_{3/2} orbital peak in the Mo–S hybrid bond structure in MoS₂ that characterized Mo⁴⁺ in MoS₂. The two weak peaks at 223.46 and 232.95 eV could be attributed to the S2s orbital and Mo–O hybrid bond structure that indicated the formation of sulfide and partial oxidation on the film surface [23]. However, the Mo–S hybrid bond of the Mo3d orbital peak of pure MoS₂ was located at the binding energies of 228.4 and 231.5 eV. The XPS spectra were consistent with the XRD and EDS results and indicated a large number of MoS₂ and Cu₃N in the heterojunction.

Figure 5 presents the energy band diagram of the Cu₃N/MoS₂ interface. The valence (VBO or ΔE_V) and conduction (CBO or ΔE_C) band offsets of the interface were calculated on the basis of the XPS spectra and corresponding band gap data as follows [13]:

$$\Delta E_V = \left(E_{\text{Cu}_3\text{N}/\text{MoS}_2}^{\text{Cu}_3\text{N}} - E_{\text{Cu}_3\text{N}/\text{MoS}_2}^{\text{Mo}_3\text{d}_{5/2}} \right) + \left(E_{\text{MoS}_2}^{\text{Mo}_3\text{d}_{5/2}} - E_{\text{VBM}}^{\text{MoS}_2} \right) - \left(E_{\text{Cu}_3\text{N}}^{\text{Cu}_3\text{N}} - E_{\text{VBM}}^{\text{Cu}_3\text{N}} \right) \quad (1)$$

$$\Delta E_C = E_g^{\text{Cu}_3\text{N}} - E_g^{\text{MoS}_2} - \Delta E_V \quad (2)$$

where E_m^s represents the energy of characteristic m in sample s , $E_{\text{VBM}}^{\text{MoS}_2}$; $E_{\text{VBM}}^{\text{Cu}_3\text{N}}$ denotes the maximum valence band values of Mo3d_{5/2} and Cu2p_{3/2} in the MoS₂ and Cu₃N samples, respectively; and $E_g^{\text{MoS}_2}$ and $E_g^{\text{Cu}_3\text{N}}$ indicate the band gap values of the MoS₂ and Cu₃N samples, respectively.

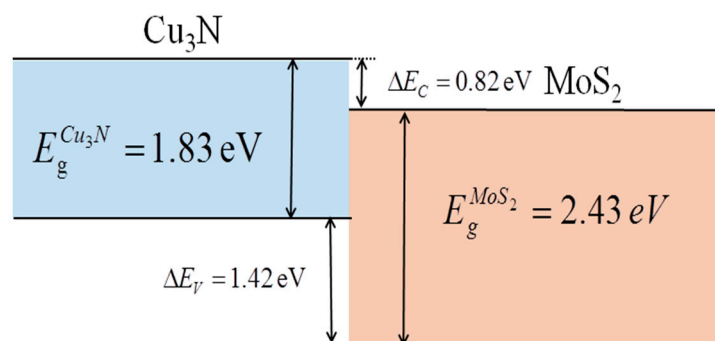


Figure 5. Band diagram of the Cu₃N/MoS₂ interface.

According to Equations (1) and (2), the VBO and CBO between the MoS₂ and Cu₃N samples were 1.42 and 0.82 eV, respectively. The band gap values of MoS₂ and Cu₃N at 2.43 and 1.83 eV, respectively, were consistent with those measured in the UV–vis transmission spectrum, and the maximum valence band values (VBM) of MoS₂ and Cu₃N were 1.15 and 1.40 eV, respectively [13]. The energy band diagram of the Cu₃N/MoS₂ heterojunction interface could be deduced on the basis of the calculated value as shown in Figure 5. The arrangement of II-type staggered band of the Cu₃N/MoS₂ heterojunction was conducive to the charge separation of electrons in the heterojunction because the Fermi level of Cu₃N was higher than that of MoS₂. After the two materials adhered to form the heterojunction, the interface electrons flowing into Cu₃N from MoS₂ increased the number of electrons in the Cu₃N layer and caused additional holes in the MoS₂ layer. These conditions

changed the optical band gap. The formed heterojunction can be applied to various high-performance photoelectric devices, such as photocatalysts and photodetectors.

The UV-vis transmission spectrum and diagram of band gap calculation of the $\text{Cu}_3\text{N}/\text{MoS}_2$ heterojunction are shown in Figure 6. The transmittance of the pure Cu_3N layer in the wavelength range of 350–650 nm was clearly improved after a heterojunction was formed between Cu_3N and MoS_2 . According to the transmission spectrum curve of the thin film, the E_g of Mo-Cu based compound region can be calculated using the optical constant law (3) and Tauc Equation (4) as follows [31]:

$$\alpha = \ln(100/T)/d \quad (3)$$

$$(\alpha h\nu)^2 = A(h\nu - E_g), \quad (4)$$

where T represents the transmittance, d denotes the film thickness, α indicates the absorption coefficient, $h\nu$ refers to the photon energy, and A signifies the constant. The band gap E_g could be inferred from the relationship curve between $(\alpha h\nu)^2$ and $h\nu$ by linearly fitting the straight part of the curve as shown in Figure 6b. The optical band gaps of the Cu_3N layer, MoS_2 layer, and $\text{Cu}_3\text{N}/\text{MoS}_2$ Mo-Cu-based compound region were 1.83, 2.43, and 1.98 eV, respectively.

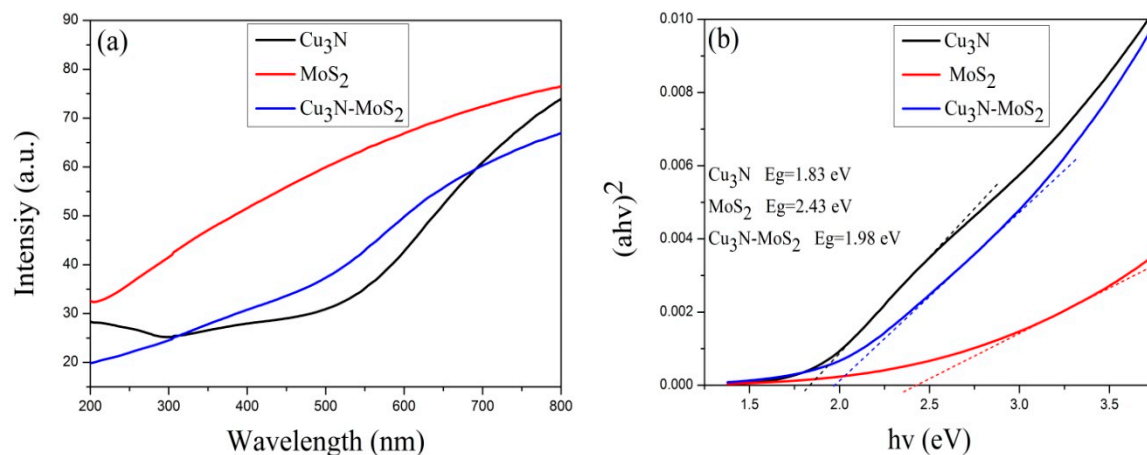


Figure 6. (a) Ultraviolet-visible (UV-vis) transmission spectrum of the $\text{Cu}_3\text{N}/\text{MoS}_2$ heterojunction and (b) determination of optical band gap of the $\text{Cu}_3\text{N}/\text{MoS}_2$ heterojunction.

4. Conclusions

$\text{Cu}_3\text{N}/\text{MoS}_2$ heterojunction was prepared on silicon and quartz substrates through magnetron sputtering. Microstructure analysis revealed the good crystallinity of MoS_2 and Cu_3N in the heterojunction, the uniform distribution of spherical grains on the surface, the thickness of the heterojunction at approximately 50 nm, and the formation of a heterojunction structure with a clear interface. This work provided a simple and effective method for preparing heterojunctions. XPS and UV correlation spectra and data revealed that the prepared $\text{Cu}_3\text{N}/\text{MoS}_2$ heterojunction had an arrangement of II-type staggered band. The VBO and CBO of the $\text{Cu}_3\text{N}/\text{MoS}_2$ interface were 1.42 and 0.82 eV, respectively. This condition facilitated the charge separation of electrons in MoS_2 . The prepared heterojunction can be applied to various high-performance photoelectric devices, such as photocatalysts and photodetectors.

Author Contributions: Formal analysis, C.G.; investigation, X.C.; writing—original draft preparation, L.Z.; writing—review and editing, Y.C. and A.J.; supervision and funding acquisition, J.X. All authors have read and agreed to the published version of the manuscript.

Funding: This research was funded by the National Natural Science Foundation of China, grant number 11364011, and the Guangxi Natural Science Foundation, grant number 2017GXNSFAA 198121.

Conflicts of Interest: The authors declare no conflicts of interest.

References

1. Nguyen, C.H.; Fu, C.-C.; Juang, R.-S. Degradation of methylene blue and methyl orange by palladium-doped TiO₂ photocatalysis for water reuse: Efficiency and degradation pathways. *J. Clean. Prod.* **2018**, *202*, 413–427. [[CrossRef](#)]
2. Yamada, N.; Maruya, K.; Yamaguchi, Y.; Cao, X.; Ninomiya, Y. p- to n-Type Conversion and Nonmetal–Metal Transition of Lithium-Inserted Cu₃N Films. *Chem. Mater.* **2015**, *27*, 8076–8083. [[CrossRef](#)]
3. Khan, S.A.; Tiwari, G.; Tripathi, R.P.; Alvi, M.A.; Khan, Z.H.; Alagel, F.A. Structural, Optical and Electrical Characterization of Polycrystalline Ga_{0.15}Te_{0.85-x}Zn_x Nano-Structured Thin Films. *Adv. Sci. Lett.* **2014**, *20*, 1715–1718. [[CrossRef](#)]
4. Han, F.; Kambala, V.S.R.; Srinivasan, M.; Rajarathnam, D.; Naidu, R. Tailored titanium dioxide photocatalysts for the degradation of organic dyes in wastewater treatment: A review. *Appl. Catal. A Gen.* **2009**, *359*, 25–40. [[CrossRef](#)]
5. Gamoudi, S.; Srasra, E. Adsorption of organic dyes by HDPy+-modified clay: Effect of molecular structure on the adsorption. *J. Mol. Struct.* **2019**, *1193*, 522–531. [[CrossRef](#)]
6. Han, J.; Jun, B.-M.; Heo, J.; Kim, S.; Yoona, Y.; Park, C.M. Heterogeneous sonocatalytic degradation of an anionic dye in aqueous solution using a magnetic lanthanum dioxide carbonate-doped zinc ferrite-reduced graphene oxide nanostructure. *Ecotoxicol. Environ. Saf.* **2019**, *182*, 109396. [[CrossRef](#)]
7. Fu, Y.; Liang, W.; Guo, J.; Tang, H.; Liu, S. MoS₂ quantum dots decorated g-C₃N₄/Ag heterojunctions for enhanced visible light photocatalytic activity. *Appl. Surf. Sci.* **2018**, *430*, 234–242. [[CrossRef](#)]
8. Wang, X.-J.; Yang, W.; Li, F.; Zhao, J.; Liu, R.; Liu, S.; Li, B. Construction of amorphous TiO₂/BiOBr heterojunctions via facets coupling for enhanced photocatalytic activity. *J. Hazard. Mater.* **2015**, *292*, 126–136. [[CrossRef](#)]
9. Peng, L.; Xie, T.; Lu, Y.; Fan, H.; Wang, D. Synthesis, photoelectric properties and photocatalytic activity of the Fe₂O₃/TiO₂ heterogeneous photocatalysts. *Phys. Chem. Chem. Phys.* **2010**, *12*, 8033–8041. [[CrossRef](#)]
10. Qu, Y.; Duan, X. Progress, challenge and perspective of heterogeneous photocatalysts. *Chem. Soc. Rev.* **2013**, *42*, 2568–2580. [[CrossRef](#)]
11. He, H.; Lin, J.; Fu, W.; Wang, X.; Wang, H.; Zeng, Q.; Gu, Q. MoS₂/TiO₂ edge-on heterojunction for efficient photocatalytic hydrogen evolution. *Adv. Energy Mater.* **2016**, *6*, 1600464. [[CrossRef](#)]
12. Low, J.; Dai, B.; Tong, T.; Jiang, C.; Yu, J. In situ irradiated X-ray photoelectron spectroscopy investigation on a direct Z-scheme TiO₂/CdS composite film photocatalyst. *Adv. Mater.* **2019**, *31*, 1802981. [[CrossRef](#)] [[PubMed](#)]
13. Su, B.; He, H.; Ye, Z. Large-area ZnO/MoS₂ heterojunction grown by pulsed laser deposition. *Mater. Lett.* **2019**, *253*, 187–190. [[CrossRef](#)]
14. Ganatra, R.; Zhang, Q. Few-Layer MoS₂: A Promising Layered Semiconductor. *ACS Nano* **2014**, *8*, 4074–4099. [[CrossRef](#)] [[PubMed](#)]
15. Gong, X.; Zhu, W.; Gong, C.M.; Xiao, J.; Zhu, L.; Wang, Z.; Ma, S. Effect of Deposition Pressure on the Microstructure and Optical Band Gap of Molybdenum Disulfide Films Prepared by Magnetron Sputtering. *Coatings* **2019**, *9*, 570. [[CrossRef](#)]
16. Cai, S.; Guo, P.; Liu, J.; Zhang, D.; Ke, P.; Wang, A.; Zhu, Y. Friction and wear mechanism of MoS₂/C composite coatings under atmospheric environment. *Tribol. Lett.* **2017**, *65*, 79. [[CrossRef](#)]
17. Chen, Q.; Li, L.L.; Peeters, F.M. Magnetic field dependence of electronic properties of MoS₂ quantum dots with different edges. *Phys. Rev. B* **2018**, *97*, 085437. [[CrossRef](#)]
18. Chen, Q.; Li, L.L.; Peeters, F.M. Inner and outer ring states of MoS₂ quantum rings: Energy spectrum, charge and spin currents. *J. Appl. Phys.* **2019**, *125*, 244303. [[CrossRef](#)]
19. Li, H.; Wu, J.; Yin, Z.; Zhang, H. Preparation and Applications of Mechanically Exfoliated Single-Layer and Multilayer MoS₂ and WSe₂ Nanosheets. *Accounts Chem. Res.* **2014**, *47*, 1067–1075. [[CrossRef](#)]
20. Chen, F.; Su, W.; Ding, S.; Fu, L. Growth and optical properties of large-scale MoS₂ films with different thickness. *Ceram. Int.* **2019**, *45*, 15091–15096. [[CrossRef](#)]
21. Baek, S.H.; Choi, Y.; Choi, W. Large-Area Growth of Uniform Single-Layer MoS₂ Thin Films by Chemical Vapor Deposition. *Nanoscale Res. Lett.* **2015**, *10*, 388. [[CrossRef](#)] [[PubMed](#)]
22. Li, H.; Zhang, G.; Wang, L. Low humidity-sensitivity of MoS₂/Pb nanocomposite coatings. *Wear* **2016**, *350*, 1–9. [[CrossRef](#)]

23. Li, H.; Li, X.; Zhang, G.; Wang, L.; Wu, G. Exploring the Tribophysics and Tribochemistry of MoS₂ by Sliding MoS₂/Ti Composite Coating Under Different Humidity. *Tribol. Lett.* **2017**, *65*, 38. [[CrossRef](#)]
24. Phung, H.N.T.; Tran, V.N.K.; Nguyen, L.T.; Phan, L.K.T.; Duong, P.A.; Le, H.V.T. Investigating visible-photocatalytic activity of MoS₂/TiO₂ heterojunction thin films at various MoS₂ deposition times. *J. Nanomater.* **2017**, *2017*. [[CrossRef](#)]
25. Phung, H.N.T.; Truong, N.D.; Duong, P.A. Influence of MoS₂ deposition time on the photocatalytic activity of MoS₂/V, N co-doped TiO₂ heterojunction thin film in the visible light region. *Curr. Appl. Phys.* **2018**, *18*, 737–743. [[CrossRef](#)]
26. Yu, A.; Ma, Y.; Chen, A.; Li, Y.; Zhou, Y.; Wang, Z.; Zhang, J.; Chu, L.; Yang, J.; Li, X. Thermal stability and optical properties of Sc-doped copper nitride films. *Vacuum* **2017**, *141*, 243–248. [[CrossRef](#)]
27. Cong, Y.; Ge, Y.; Zhang, T.; Wang, Q.; Shao, M.; Zhang, Y. Fabrication of Z-Scheme Fe₂O₃–MoS₂–Cu₂O Ternary Nanofilm with Significantly Enhanced Photoelectrocatalytic Performance. *Ind. Eng. Chem. Res.* **2018**, *57*, 881–890. [[CrossRef](#)]
28. Pierson, J.; Horwat, D. Addition of silver in copper nitride films deposited by reactive magnetron sputtering. *Scr. Mater.* **2008**, *58*, 568–570. [[CrossRef](#)]
29. Li, J.; Yao, C.; Kong, X.; Li, Z.; Jiang, M.; Zhang, F.; Lei, X. Boosting Hydrogen Production by Electrooxidation of Urea over 3D Hierarchical Ni₄N/Cu₃N Nanotube Arrays. *ACS Sustain. Chem. Eng.* **2019**, *7*, 13278–13285. [[CrossRef](#)]
30. Jiang, A.; Qi, M.; Xiao, J. Preparation, structure, properties, and application of copper nitride (Cu₃N) thin films: A review. *J. Mater. Sci. Technol.* **2018**, *34*, 1467–1473. [[CrossRef](#)]
31. Xiao, J.; Qi, M.; Cheng, Y.; Jiang, A.; Zeng, Y.; Ma, J. Influences of nitrogen partial pressure on the optical properties of copper nitride films. *RSC Adv.* **2016**, *6*, 40895–40899. [[CrossRef](#)]
32. Cremer, R.; Witthaut, M.; Trappe, C.; Laurenzis, M.; Winkler, O.; Kurz, H.; Neuschütz, D. Deposition and Characterization of Metastable Cu₃N Layers for Applications in Optical Data Storage. *Microchim. Acta* **2000**, *133*, 299–302. [[CrossRef](#)]
33. Jiang, A.; Xiao, J.; Gong, C.; Wang, Z.; Ma, S. Structure and electrical transport properties of Pb-doped copper nitride (Cu₃N:Pb) films. *Vacuum* **2019**, *164*, 53–57. [[CrossRef](#)]
34. Soares, L.; Alves, A. Photocatalytic properties of TiO₂ and TiO₂/WO₃ films applied as semiconductors in heterogeneous photocatalysis. *Mater. Lett.* **2018**, *211*, 339–342. [[CrossRef](#)]
35. Ye, M.; Zhang, G.-J.; Ba, Y.; Wang, T.; Wang, X.; Liu, Z. Microstructure and tribological properties of MoS₂+Zr composite coatings in high humidity environment. *Appl. Surf. Sci.* **2016**, *367*, 140–146. [[CrossRef](#)]



© 2020 by the authors. Licensee MDPI, Basel, Switzerland. This article is an open access article distributed under the terms and conditions of the Creative Commons Attribution (CC BY) license (<http://creativecommons.org/licenses/by/4.0/>).